 CMES, vol.69, no.3, pp.199-221, 2010

An Atom-Based Continuum Method for Multi-element Crystals at Nano Scale

Xianqiao Wang[1] and James D. Lee[2]

Abstract: This paper presents an atom-based continuum (ABC) method aiming at a seamless transition from the atomistic to the continuum description of multi-element crystalline solids (which has more than one kind of atom in the unit cell). Contrary to many concurrent multiscale approaches, ABC method is naturally suitable for the analysis of multi-element crystals within a finite element (FE) framework. Taking both efficiency and accuracy into account, we adopt a cluster-based summation rule for atomic force calculations in the FE formulations. Single-crystals MgO, $BaTiO_3$ and Cu under mechanical loading are modeled and simulated. With a coarse-grained mesh, ABC method is shown to be able to simulate dynamic and nonlinear behaviors, such as wave propagation and polarization, of multi-element crystalline materials. It is demonstrated that by reducing the finite element mesh to the atomic scale, in other words, let the finite element size equal to the size of a unit cell, critical phenomena at atomic scale such as crack propagation can be successfully reproduced.

Keywords: Multiscale material modeling, Molecular dynamics, Finite element method, Multi-element crystals, Critical phenomena

1 Introduction

For several decades continuum theory has been a dominating theoretical framework for the analysis of materials and structures. It is realized that as technologies extend to the nanometer range, continuum mechanics at this new arena is questionable. While atomic-scale modeling and simulation methods, e.g., molecular dynamics (MD), have provided a wealth of information for nano systems, these methods can only handle problems limited in length/time scales. Yet, ultimately we aim at the

[1] Department of Mechanical and Aerospace Engineering, George Washington University, Washington, DC 20052 xqwang@gwmail.gwu.edu.

[2] Department of Mechanical and Aerospace Engineering, George Washington University, Washington, DC 20052 jdlee@gwu.edu

design and manufacture of synthetic and hierarchical material systems or structures in which the organization is designed and controlled on length scales ranging from nanoscopic to microscopic, even to macroscopic. Therefore multiscale modeling, from atom to continuum, is inevitably needed.

The past several years have witnessed the explosive growth of interest in theory and modeling of microscale, nanoscale and multiscale material behaviors. One of the most popular concurrent multiscale modeling approaches is to incorporate a hand shaking region between the FE and the MD regions. To begin with, the coupling of length scale method (CLSM) was a pioneering work developed by Abraham et al. (1998), and by Rudd and Broughton (2001), which incorporated the coupling of quantum mechanics approximation, MD, and FE method. Belytschko and Xiao (2003), Xiao and Belytschko (2004) developed the bridging-domain method (BDM), in which the continuum and molecular domains were overlapped in a bridging subdomain, and the Hamiltonian was taken to be the linear combination of the continuum and molecular parts. The compatibility in BDM was enforced by Method of Lagrange multipliers. Wagner and Liu (2003) developed the bridging scale method (BSM), in which the molecular displacements were decomposed into fine and coarse scales. At the interface they used a form of the Langevin equation to eliminate spurious reflections. Excellent result for one-dimensional problem was obtained. The atomistic-to-continuum (AtC) method by Fish et al. (2007) and by Parks et al. (2008) was a force-based method in which the coupling between atomistic and continuum regions was achieved by blending at the level of forces. In these fashions, the computational power is harnessed, resulting in an optimum compromise between numerical accuracy and computational overhead. The multiscale simulation technique based on the meshless local Petrov-Galerkin method was developed by Shen and Atluri (2004 a, b, c), in which several alternate time-dependent interfacial conditions, between the atomistic and continuum regions, are systematically studied, for the seamless multiscale simulation, by decomposing the displacement of atoms in the equivalent continuum region into long and short wave-length components. Ma et al. (2006) also developed a multiscale simulation method using generalized interpolation material point method (GIMP) and molecular dynamics. In their theory, a material point in the continuum is split into smaller material points using multi-level refinement until it has nearly reached the atom size to couple with atoms in the MD region. Consequently, coupling between GIMP and MD is achieved by using compatible deformation, force, and energy fields in the transition region between GIMP and MD. Raghavan and Ghosh (2004) established an adaptive multiscale computational modeling of composite materials that combines a conventional displacement based finite element model with a microstructural Voronoi cell finite element model for multi-scale analysis

of composite structures with non-uniform microstructural heterogeneities as obtained from optical or scanning electron micrographs. Compared with direct atomistic simulation, these techniques have the potential to produce significant time and length scale gains by treating smoothly varying regions of the configurational space collectively. Generally speaking, however, in all those above-mentioned coupled methods, the idea is to use a fully atomistic description in the critical regions and a continuum description in other regions, thereby resulting in a phonon scattering and wave reflection at the interface. Also, the detailed treatment of the material in the 'transition region' or the boundary between the atomistic and continuum regions is a critical aspect of those approaches.

Another popular bottom-up approach is the Quasicontinuum (QC) method, developed by Tadmor et al. (1996) and extended by Knap and Ortiz (2001). In QC method, triangular elements or tetrahedral elements are adopted in 2D or 3D simulations, respectively, thereby leading to a locally-uniform deformation gradient. Linear interpolation functions in triangular or tetrahedral elements require only one Gauss-point for numerical quadrature. As a consequence, the application of the Cauchy-Born rule (CBR) implies that in the energy calculation the summation over the number of lattice sites boils down to the number of finite elements. Therefore, there will be a limitation for QC method due to the validity of the kinematic assumption of CBR; in other words, QC method is unable to determine the state when the non-affine deformation is possible due to instabilities or inhomogeneities of the underlying atomic system (Stienmann et al., 2006). One has to mention that Tadmor et al. (1999) extended the QC method to simulate materials with multiple atoms in a unit cell. However, from the view point of practice and efficiency, we have to say that the Cauchy-Born rule certainly is not appropriate for materials with multiple atoms in a unit cell.

In this paper, we propose an atom-based continuum (ABC) method aiming at a seamless transition from the atomistic to the continuum description of crystalline solids and a general formulation for the analysis of multi-element crystals. Each unit cell of a multi-element crystal has multiple discrete and distinct atoms. To enhance the computational efficiency, we present a cluster-based force calculation rule in the FE formulation. The organization of the remainder of the paper is as follows: In Section 2, we briefly present basic concepts of lattice dynamics and derive the governing equations of atomic system based on the generalized Lagrange equation. By means of virtual work and kinematic constraints, in Section 3 we formulate the atom-based continuum method and its derivative —-the concurrent atomistic/continuum method. Coarse-grained and concurrent atomistic/continuum simulation results are presented in Section 4 and 5, respectively. Finally we conclude this paper with a brief summary and discussion in Section 6.

2 Lattice Dynamics

Note that a crystalline material is distinguished from other states of matter by a periodic arrangement of the atoms, which can be represented as a collection of unit cells and a group of discrete and distinct atoms situated within each unit cell as depicted in Fig. 1. Consider a system consisting of N_l unit cells; each unit cell k is composed of N_a atoms with mass m^α $[\alpha = 1,2,3,....,N_a]$, positions in the reference configuration $\mathbf{X}^{k\alpha}$, positions in the current configuration $\mathbf{x}^{k\alpha}(t)$, displacements $\mathbf{u}^{k\alpha}(t) = \mathbf{x}^{k\alpha}(t) - \mathbf{X}^{k\alpha}$, and velocities $\dot{\mathbf{u}}^{k\alpha}(t)$. Herein, the superscript $k\alpha$ refers to the αth atom in the kth unit cell; and $\dot{\mathbf{u}}^{k\alpha} \equiv d\mathbf{u}^{k\alpha}/dt$.

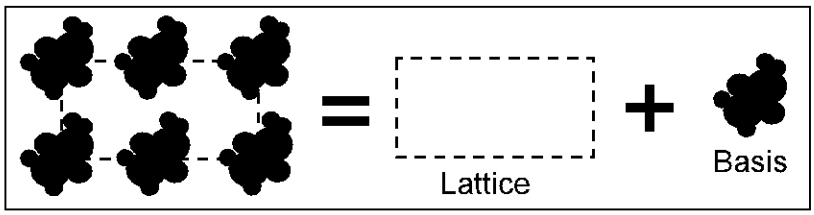

Figure 1: Atomistic view of crystal structure

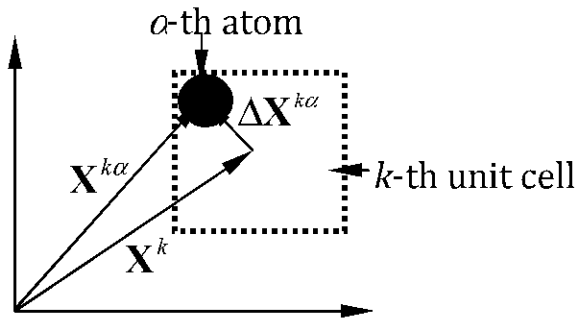

Figure 2: Position descriptions in the reference configuration

The initial configuration of each unit cell in a single crystalline material can be identified by its lattice coordinates $k = (k_1, k_2, \cdots, k_d) \in Z^d$, where d denotes the dimensions of space. So the spatial initial position $\mathbf{X}^k$ of the kth unit cell is defined as

$$\mathbf{X}^k = \sum_{a=1}^{d} k_a \mathbf{B}_a \tag{1}$$

where $\mathbf{B}_a$ are the basis vectors spanning a simple d-dimensional Bravais lattice.

The positions, shown in Fig. 2, in the reference configuration, displacements and velocities between atoms and the center of the unit cell are

$$\mathbf{X}^{k\alpha} = \mathbf{X}^k + \Delta\mathbf{X}^{k\alpha} \tag{2}$$

$$\mathbf{u}^{k\alpha}(t) = \mathbf{u}^k(t) + \Delta\mathbf{u}^{k\alpha}(t) \tag{3}$$

$$\dot{\mathbf{u}}^{k\alpha}(t) = \dot{\mathbf{u}}^k(t) + \Delta\dot{\mathbf{u}}^{k\alpha}(t) \tag{4}$$

where $\Delta\mathbf{X}^{k\alpha}$, $\Delta\mathbf{u}^{k\alpha}$, and $\Delta\dot{\mathbf{u}}^{k\alpha}$ are the internal positions, the internal displacements and the internal velocities of the αth atom in the kth unit cell, respectively. The unit cell deformation $\mathbf{u}^k(t)$ is homogenous while the internal displacement $\Delta\mathbf{u}^{k\alpha}(t)$ contributes to inhomogeneous deformation.

It is assumed that the total potential energy V of the system mentioned above can be additively computed as the sum of energies of each atom

$$V = \sum_k \sum_\alpha V^{k\alpha} \tag{5}$$

where $V^{k\alpha}$ is the sum of the energies due to any interatomic potential, such as pair-wise interaction of the atoms, three-body potentials or other many-body potentials, including the Tersoff and the Stillinger-Weber potentials. $V^{k\alpha}$ can be expressed in a general form

$$V^{k\alpha} = \frac{1}{2!}\sum_l \sum_\beta V_2(\mathbf{x}^{k\alpha}, \mathbf{x}^{l\beta}) + \frac{1}{3!}\sum_{l,m} \sum_{\beta,\gamma} V_3(\mathbf{x}^{k\alpha}, \mathbf{x}^{l\beta}, \mathbf{x}^{m\gamma}) + \cdots \tag{6}$$

with the understanding $(k,\alpha) \neq (l,\beta) \neq (m,\gamma) \neq .....$

The particular form of the interatomic potential energy depends on the model of atomic interactions. In this work, we assume pair potential is employed and the potential energy of the atom $k\alpha$ is

$$V^{k\alpha} = \frac{1}{2}\sum_l \sum_\beta V_2(\mathbf{x}^{k\alpha}, \mathbf{x}^{l\beta}) \equiv \frac{1}{2}\sum_l \sum_\beta V^{k\alpha - l\beta}(\mathbf{x}^{k\alpha}, \mathbf{x}^{l\beta}) \tag{7}$$

Let the kinetic energy and the dissipative energy of this system be

$$K = \frac{1}{2}\sum_k \sum_\alpha m^\alpha (\dot{\mathbf{x}}^{k\alpha})^2 \tag{8}$$

$$D = \{\frac{1}{2}\sum_k \sum_\alpha m^\alpha (\dot{\mathbf{x}}^{k\alpha})^2\}/\tau \tag{9}$$

where D is ordinarily known as Rayleigh's dissipation function and represents the rate at which mechanical energy is converted to heat during a viscous process; τ is a characteristic damping time (Goldstein, 1950).

We start from the generalized Lagrange equation for holonomic non-conservative systems, in which non-potential forces exist:

$$\frac{d}{dt}\left(\frac{\partial L}{\partial \dot{\mathbf{x}}}\right)-\frac{\partial L}{\partial \mathbf{x}}+\frac{\partial D}{\partial \dot{\mathbf{x}}}=\varphi(\mathbf{x},\dot{\mathbf{x}},t) \tag{10}$$

where $L(\mathbf{x},\dot{\mathbf{x}},t)=K-V$ is the Lagrangian and $\varphi(\mathbf{x},\dot{\mathbf{x}},t)$ is the generalized non-potential forces.

Substituting Eqs. (7, 8, 9) into Eq. (10) and assuming that the forces on any atom are additive, we have the governing equation of any atom $k\alpha$ in the system with damping (see the details in Appendix A)

$$m^{\alpha}\ddot{\mathbf{u}}^{k\alpha}+c^{\alpha}\dot{\mathbf{u}}^{k\alpha}=\mathbf{f}^{k\alpha}+\varphi^{k\alpha} \tag{11}$$

where $\dot{\mathbf{u}}^{k\alpha}=\dot{\mathbf{x}}^{k\alpha}$; $\ddot{\mathbf{u}}^{k\alpha}=\ddot{\mathbf{x}}^{k\alpha}$; $c^{\alpha}\equiv m^{\alpha}/\tau$; $\mathbf{f}^{k\alpha}=\sum_l\sum_\beta \mathbf{f}^{k\alpha-l\beta}$; $\varphi^{k\alpha}$ is the external force acting on the $k\alpha$ atom; $\mathbf{f}^{k\alpha-l\beta}$ is the atomic force acting on the $k\alpha$ atom due to the $l\beta$ atom, which is the negative derivative of the potential energy $V^{k\alpha-l\beta}(\mathbf{x}^{k\alpha},\mathbf{x}^{l\beta})$ with respect to the atom's current position vector $\mathbf{x}^{k\alpha}$

$$\mathbf{f}^{k\alpha-l\beta}=-\frac{\partial V^{k\alpha-l\beta}(\mathbf{x}^{k\alpha},\mathbf{x}^{l\beta})}{\partial \mathbf{x}^{k\alpha}} \tag{12}$$

and here we also assume that the potential energies depend only on the relative interatomic distance $d^{k\alpha-l\beta}=\left\|\mathbf{x}^{k\alpha}-\mathbf{x}^{l\beta}\right\|$, so

$$\mathbf{f}^{k\alpha-l\beta}=-\frac{\partial V^{k\alpha-l\beta}(d^{k\alpha-l\beta})}{\partial d^{k\alpha-l\beta}}\frac{\partial d^{k\alpha-l\beta}}{\partial \mathbf{x}^{k\alpha}}=-\frac{\partial V^{k\alpha-l\beta}(d^{k\alpha-l\beta})}{\partial d^{k\alpha-l\beta}}\frac{\mathbf{x}^{k\alpha}-\mathbf{x}^{l\beta}}{d^{k\alpha-l\beta}}=-\mathbf{f}^{l\beta-k\alpha} \tag{13}$$

3 Atom-Based Continuum Method (ABC)

3.1 Kinematic constrains

For the purpose of large-scale simulation of collaborative material behavior, we seek an approximation solution to Eq. (11). Therefore, following the work done by Knap and Ortiz (2001) and the work done by Eidel and Stukowski (2009), the reduction of degrees of freedom is accomplished by virtue of kinematic constrains. i.e., the shape functions in FE method. Some judiciously selected unit cells, called

FE nodes, retain their independent degrees of freedom. Z is the set of all unit cells; Z_N is the set of all FE nodes; $Z_N \subseteq Z$. The nodal displacements together with shape functions are employed to determine a displacement field, in other words, all other unit cells are forced to follow the motion of the nodes – this is what we called "kinematic constraint", which is the practice in every FE analysis. The most general requirements to the discretization are first, to reduce the number of FE node, and second, to ensure high density of FE nodes up to fully atomic resolution in critical regions, where defects nucleate and evolve, like dislocation cores, crack tips. When coarse mesh is used, the majority of the degrees of freedom can be eliminated, hence, the computational cost can be reduced. When the finest mesh is used, any lattice site is a finite element node, and the model becomes identical to a full-blown MD model. The compromise is a trade-off between efficiency and accuracy (Eidel and Stukowski, 2009). The density of FE nodes is controlled by a criterion that measures how strong the deformation varies spatially. The displacement $\mathbf{u}^{k\alpha}$ is approximated by finite element interpolation from its nodal values $\mathbf{U}_I^{\alpha}$ as

$$\mathbf{u}^{k\alpha} = \sum_I \Phi_I(k)\mathbf{U}_I^{\alpha} \tag{14}$$

where $\Phi_I(k)$ is I-th shape function of the kth unit cell; $\mathbf{U}_I^{\alpha}$ is the displacements of the α atom of the I-th node of the element in which the kth unit cell resides. The finite element shape functions exhibit the properties

$$\sum_I \Phi_I(k) = 1 \tag{15}$$

$$\Phi_I(j) = \delta_{Ij} \quad \forall\, j \in Z_N \tag{16}$$

According to Eq. (15) shape functions are a partition of unity over Z, which ensures the exact representation of constant fields.

Following the standard procedure of Galerkin method, we have the weak form of Eq. (11) as follows

$$\sum_k \sum_\alpha m^\alpha \ddot{\mathbf{u}}^{k\alpha} \delta\mathbf{u}^{k\alpha} + \sum_k \sum_\alpha c^\alpha \dot{\mathbf{u}}^{k\alpha} \delta\mathbf{u}^{k\alpha} = \sum_k \sum_\alpha \sum_l \sum_\beta \mathbf{f}^{k\alpha - l\beta} \delta\mathbf{u}^{k\alpha} + \sum_k \sum_\alpha \varphi^{k\alpha} \delta\mathbf{u}^{k\alpha} \tag{17}$$

In light of $\mathbf{f}^{k\alpha - l\beta} = -\mathbf{f}^{l\beta - k\alpha}$, we rewrite Eq. (17) as

$$\sum_k \sum_\alpha m^\alpha \ddot{\mathbf{u}}^{k\alpha} \delta\mathbf{u}^{k\alpha} + \sum_k \sum_\alpha c^\alpha \dot{\mathbf{u}}^{k\alpha} \delta\mathbf{u}^{k\alpha} = \frac{1}{2} \sum_k \sum_\alpha \sum_l \sum_\beta \{\mathbf{f}^{k\alpha - l\beta} - \mathbf{f}^{l\beta - k\alpha}\} \delta\mathbf{u}^{k\alpha} + \sum_k \sum_\alpha \varphi^{k\alpha} \delta\mathbf{u}^{k\alpha} \tag{18}$$

which can also be written as

$$\sum_k \sum_\alpha m^\alpha \ddot{\mathbf{u}}^{k\alpha} \delta \mathbf{u}^{k\alpha} + \sum_k \sum_\alpha c^\alpha \dot{\mathbf{u}}^{k\alpha} \delta \mathbf{u}^{k\alpha} = \frac{1}{2} \sum_k \sum_\alpha \sum_l \sum_\beta \mathbf{f}^{k\alpha - l\beta} \{ \delta \mathbf{u}^{k\alpha} - \delta \mathbf{u}^{l\beta} \} + \sum_k \sum_\alpha \varphi^{k\alpha} \delta \mathbf{u}^{k\alpha} \quad (19)$$

By virtue of $\delta \mathbf{u}^{k\alpha} = \sum_I \Phi_I(k) \delta \mathbf{U}_I^\alpha$, the governing equations for nodal displacements $\mathbf{U}_I^\alpha$ can be expressed(see the detail in Appendix B)

$$\left(\sum_J M_{IJ}^\alpha \right) \ddot{\mathbf{U}}_J^\alpha + \left(\sum_J C_{IJ}^\alpha \right) \dot{\mathbf{U}}_J^\alpha = \mathbf{F}_I^\alpha + \varphi_I^\alpha \quad (20)$$

where

$$M_{IJ}^\alpha = \sum_k m^\alpha \Phi_J(k) \Phi_I(k) = M_{JI}^\alpha \quad (21)$$

$$C_{IJ}^\alpha = \sum_k c^\alpha \Phi_J(k) \Phi_I(k) = C_{JI}^\alpha \quad (22)$$

$$\mathbf{F}_I^\alpha = \frac{1}{2} \sum_k \sum_l \sum_\beta \mathbf{f}^{k\alpha - l\beta} \Phi_I(k) - \frac{1}{2} \sum_k \sum_l \sum_\gamma \mathbf{f}^{k\gamma - l\alpha} \Phi_I(l) \quad (23)$$

$$\varphi_I^\alpha = \sum_k \varphi^{k\alpha} \Phi_I(k) \quad (24)$$

The existence of superscript α in Eq. (20) implies that the atomic information is naturally built in ABC method and the internal relaxation is allowed in each node to represent an atomistic multi-element system, thereby eliminating the mismatch of phonon descriptions in atomic and continuum regions. Hence ABC is inherently suitable for the study of polarizations and phase transformations in multi-element crystals at continuum level. This is distinctively different from the classical continuum field theory. It is also noticed that, in Eqs. (23, 24), full-blown nonlocality, nonlinearity and atom-based constitutive relation are automatically rooted in the force calculation. So we have proposed a fully nonlocal ABC formulation.

In practice, the consistent mass matrix is commonly replaced by a lumped matrix for computational convenience. Here we utilize the 'row-sum' lumping technique, then Eq. (20) can be rewritten as

$$\tilde{M}_I^\alpha \ddot{\mathbf{U}}_I^\alpha + \left(\sum_J C_{IJ}^\alpha \right) \dot{\mathbf{U}}_J^\alpha = \mathbf{F}_I^\alpha + \varphi_I^\alpha \quad (25)$$

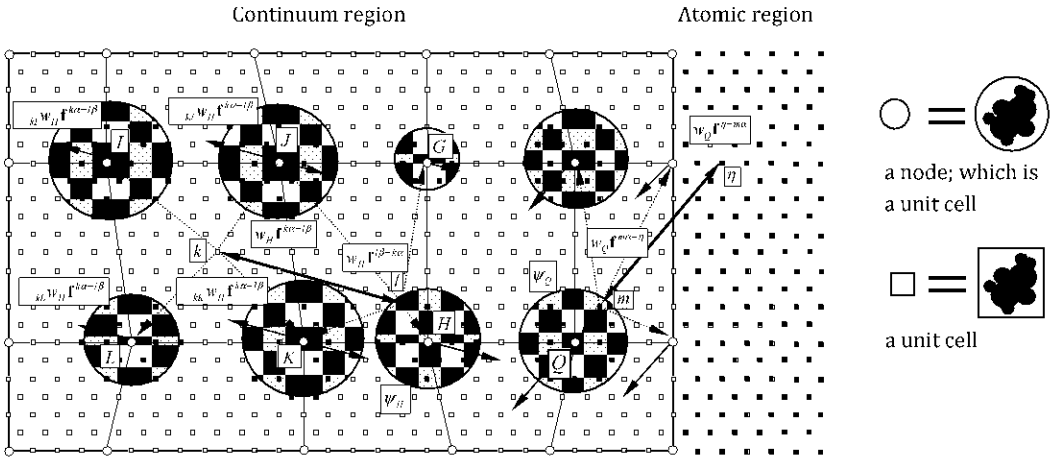

Figure 3: Schematic picture of ABC model with force distributions

If we consider that the specimen has two regions: continuum region (N_l unit cells; each unit cell has N_a atoms) with finite element meshes and atomic region (N atoms), as shown in Fig. 3 (here a 2D picture is shown for the purpose of illustration), we can extend ABC method to a **concurrent atomistic/continuum** method. Then the governing equations of this composite system can be expressed as:

Continuum region $[\alpha = 1,2,3,\cdots,N_a]$

$$\tilde{M}_I^\alpha \ddot{\mathbf{U}}_I^\alpha + \left(\sum_J C_{IJ}^\alpha\right)\dot{\mathbf{U}}_J^\alpha = \mathbf{F}_I^\alpha + \varphi_I^\alpha \tag{26}$$

where the interatomic force $\mathbf{F}_I^\alpha$ is a little bit different from Eq. (23) because we should include the interaction with atoms in the atomic region:

$$\mathbf{F}_I^\alpha = \frac{1}{2}\sum_k\sum_l\sum_\beta \mathbf{f}^{k\alpha-l\beta}\Phi_I(k) - \frac{1}{2}\sum_k\sum_l\sum_\gamma \mathbf{f}^{k\gamma-l\alpha}\Phi_I(l) + \sum_k\sum_{\eta=1}^{N}\mathbf{f}^{k\alpha-\eta}\Phi_I(k) \tag{27}$$

The diagonalized mass matrix $\tilde{M}_I^\alpha$, the damping matrix C_{IJ}^α and the external force φ_I^α are the same as Eqs. (21, 22, 24).

Atomic region $[\eta = 1,2,3,\cdots,N]$

$$m^\eta \ddot{\mathbf{u}}^\eta(t) = \mathbf{F}^\eta(t) + \mathbf{\Phi}^\eta(t) \tag{28}$$

where $\mathbf{\Phi}^\eta(t)$ is the external force acting on the ηth atom; and the interatomic force acting on the ηth atom $\mathbf{F}^\eta(t)$ is

$$\mathbf{F}^\eta = \sum_k\sum_\alpha \mathbf{f}^{\eta-k\alpha} + \sum_\xi \mathbf{f}^{\eta-\xi} \tag{29}$$

3.2 Summation rule for force calculation

All summations in Eqs. (21-24, 27, 29) are normally carried out by numerical quadrature. In Fig. 3, it is seen that around each node (an open circle), say the kth node, there is a cluster (a shaded area), named ψ_k. From now on, force calculation is no longer performed for all unit cells in the entire system but for all clusters. A representative unit cell (a black solid square) is the one within one of $\psi_k = \{l : |\mathbf{X}_l - \mathbf{X}_k| \leq R_k\}$. Notice that there is no overlapping of clusters. $\mathbf{X}_l$ is the position of the lth unit cell and R_k is the radius of the cluster ψ_k centered at the kth unit cell, which happens to be a FE node. We postulate that the cluster summation rule for Eq. (27) reads:

$$\begin{aligned}
\mathbf{F}_J^{\alpha} &= \frac{1}{2}\sum_k\sum_l\sum_\beta \mathbf{f}^{k\alpha-l\beta}\mathbf{\Phi}_J(k) - \frac{1}{2}\sum_k\sum_l\sum_\gamma \mathbf{f}^{k\gamma-l\alpha}\mathbf{\Phi}_J(l) + \sum_k\sum_{\eta=1}^{N}\mathbf{f}^{k\alpha-\eta}\mathbf{\Phi}_J(k) \\
&\approx \frac{1}{2}\sum_{i\in Z_N}^{w_i}\sum_{j\in\psi_i}\sum_{l=1}^{N_l}\sum_{\beta=1}^{N_a}\mathbf{f}^{j\alpha-l\beta}\mathbf{\Phi}_J(j) - \frac{1}{2}\sum_{i\in Z_N}^{w_i}\sum_{j\in\psi_i}\sum_{l=1}^{N_l}\sum_{\gamma=1}^{N_a}\mathbf{f}^{j\gamma-l\alpha}\mathbf{\Phi}_J(l) \\
&+ \sum_{i\in Z_N}^{w_i}\sum_{j\in\psi_i}\sum_{\eta=1}^{N}\mathbf{f}^{j\alpha-\eta}\mathbf{\Phi}_J(j)
\end{aligned} \tag{30}$$

where $w_i (i \in Z_N)$, the weight of the ith cluster, is calculated under the requirement that the summation over all linear interpolation functions must be exact, see Knap and Ortiz (2001); Eidel and Stukowski (2009). When the clusters shrink to nodes, i.e., $\psi_i = \{i\} \ \forall\, i \in Z_N$, it holds $\mathbf{\Phi}_I(i) = \delta_{Ii}$, and the cluster summation rule boils down to a node-based summation rule

$$\mathbf{F}_J^{\alpha} \approx \frac{1}{2}\sum_{i\in Z_N}^{w_i}\sum_{l=1}^{N_l}\sum_{\beta=1}^{N_a}\delta_{Ji}\mathbf{f}^{i\alpha-l\beta} - \frac{1}{2}\sum_{i\in Z_N}^{w_i}\sum_{l=1}^{N_l}\sum_{\gamma=1}^{N_a}\mathbf{f}^{i\gamma-l\alpha}\mathbf{\Phi}_J(l) + \sum_{i\in Z_N}^{w_i}\sum_{\eta=1}^{N}\mathbf{f}^{i\alpha-\eta}\delta_{Ji} \tag{31}$$

In this case the weighting factor w_i is the number of unit cells represented by ith node, thus $w_i = \sum_{j=1}^{N_l}\mathbf{\Phi}_i(j) \ \ \forall i \in Z_N$. On the other extreme, $w_i = 1 \forall\, i \in Z_N$ implies all pairs of interatomic forces are calculated. In all cases $\sum_{i\in Z_N}\sum_{j\in\psi_i} w_j = N_l$ holds. Fig. 3 shows the numerical procedures to calculate the interatomic force between any two atoms. The force between any two atoms in the atomic region is treated exactly the same way as in MD simulation. In the continuum region the force between any two atoms in different or same unit cells should be distributed to all the nodes of the elements, in which the two unit cells reside. For example, there is a unit cell l located in cluster ψ_H with weighting factor w_H and another generic unit cell k; $\{\mathbf{f}^{k\alpha-l\beta}, \mathbf{f}^{l\beta-k\alpha}\}$ represents a pair of interatomic forces acting on the $k\alpha$th

atom and the $l\beta$th atom, $\mathbf{f}^{k\alpha-l\beta} = -\mathbf{f}^{l\beta-k\alpha}$; through shape function $\mathbf{\Phi}_{kI} = \mathbf{\Phi}_I(k)$, force $w_H\mathbf{\Phi}_{kI}\mathbf{f}^{k\alpha-l\beta}$ is distributed to the αth atom of node I; similarly, $w_H\mathbf{\Phi}_{kJ}\mathbf{f}^{k\alpha-l\beta}$, $w_H\mathbf{\Phi}_{kK}\mathbf{f}^{k\alpha-l\beta}$, and $w_H\mathbf{\Phi}_{kL}\mathbf{f}^{k\alpha-l\beta}$ are distributed to the αth atom of nodes J, K, and L; in the same way, $w_H\mathbf{\Phi}_{lJ}\mathbf{f}^{l\beta-k\alpha}$, $w_H\mathbf{\Phi}_{lK}\mathbf{f}^{l\beta-k\alpha}$, $w_H\mathbf{\Phi}_{lG}\mathbf{f}^{l\beta-k\alpha}$ and $w_H\mathbf{\Phi}_{lH}\mathbf{f}^{l\beta-k\alpha}$ are distributed to the βth atom of nodes J, K, G, and H. Let $\{\mathbf{f}^{m\alpha-\eta}, \mathbf{f}^{\eta-m\alpha}\}$ represent a pair of interatomic forces acting on the $m\alpha$th atom in the continuum region and the ηth atom in the atomic region.

In this work, we investigate the mechanical behaviors of single-crystals MgO, $BaTiO_3$, and Cu (Fig. 4) in the following sections. For the ionic MgO and $BaTiO_3$ crystals, the Coulomb-Buckingham potentials listed in Table 1 and 2 (Grimes, 1994; Woodley, 1999) are adopted to derive the interatomic force, respectively, while the Lennard-Jones potential listed in Table 3 is used for Cu.

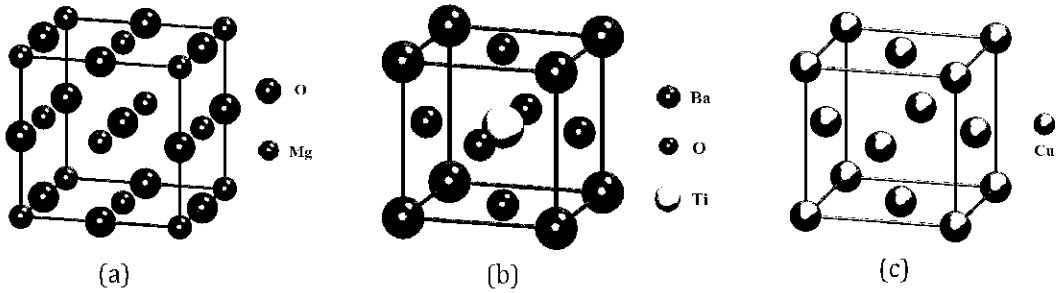

Figure 4: Crystal structures: (a) MgO; (b)$BaTiO_3$; (c)Cu

Table 1: Short-range interaction parameters for different pairs in MgO

Species	Species	A (eV)	ρ (Å)	C (eV(Å)^6)
O^{2-}	O^{2-}	9547.96	0.2192	32.0
Mg^{2+}	O^{2-}	1284.38	0.2997	0.00
Mg^{2+}	Mg^{2+}	0.00000	0.0000	0.00

4 Coarse-scale simulations of ABC method

4.1 Wave propagation

Consider that a uniaxial compressive loading is applied on both two ends of a Cu specimen (2.9 nm × 2.9 nm × 22 nm, 19,764 atoms) along the z-direction (cf. Fig. 5). The displacement $U_z$specified at the boundary is increased to 0.9nm in a linear

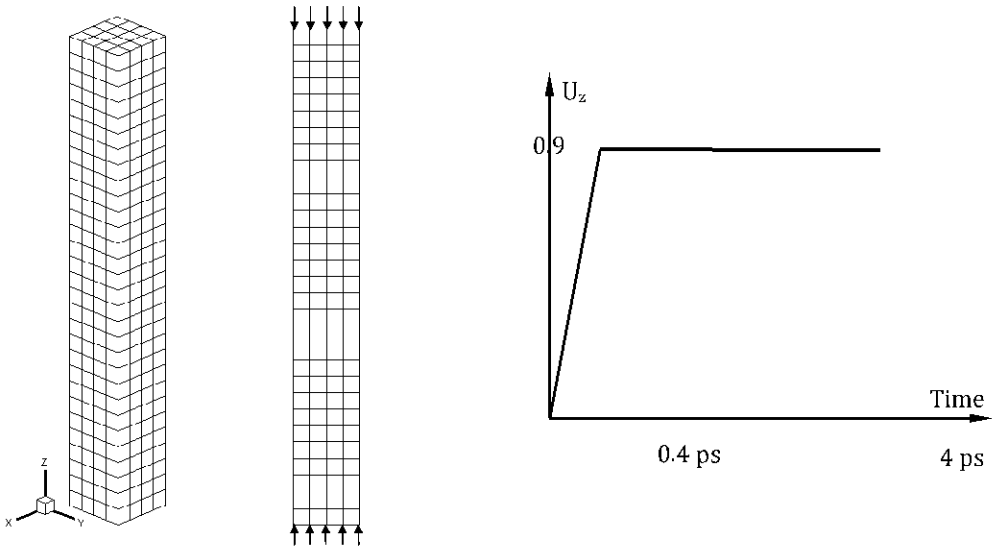

Figure 5: Computational model of Cu specimen under a compressive loading

Table 2: Short-range interaction parameters for different pairs in $BaTiO_3$

Species	Species	A (eV)	ρ (Å)	C (eV(Å)^6)
O^{2-}	O^{2-}	25.4100	0.6937	32.32
Ba^{2+}	O^{2-}	4818.42	0.3067	0.000
Ti^{2+}	O^{2-}	4545.82	0.2610	0.000
Ba^{2+}/Ti^{2+}	Ba^{2+}/Ti^{2+}	0.00000	0.0000	0.000

Table 3: Short-range interaction parameters for Cu

Species	Species	ε (eV)	σ (Å)
Cu	Cu	0.415	2.277

ramp over 0.4 ps. Thereafter, the displacements on the two ends are held as constant at 0.9 nm. Fig. 5 shows the computational model, loading history and the boundary conditions. Uniform 3D 8-node brick-type elements are employed, and there are 480 elements and 775 nodes in the FE model. Approximately, the number of degrees of freedom involved in ABC is about 4% of that of MD.

Fig. 6 shows the contour plots of displacement U_x in deformed shape as well as in atomic arrangement. Wave propagation along the $z$direction is clearly observed. It is also seen that, under the compressive loading, the bulging in x-direction develops just beneath the boundaries. The bulging originates from two ends, propa-

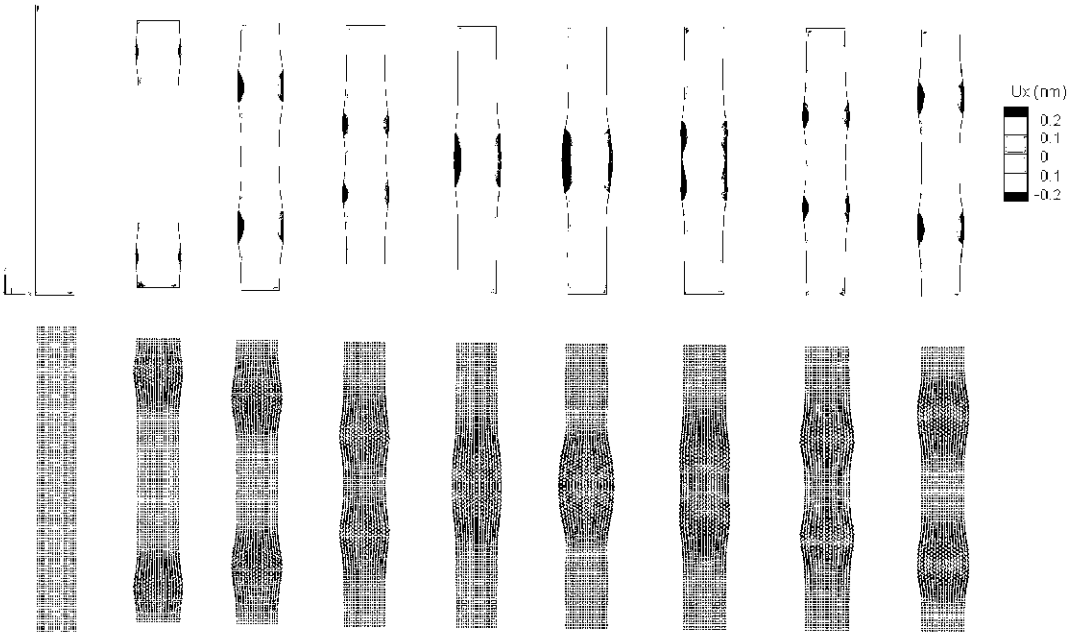

Figure 6: Distribution of U_x in deformed shape and in atomic arrangement

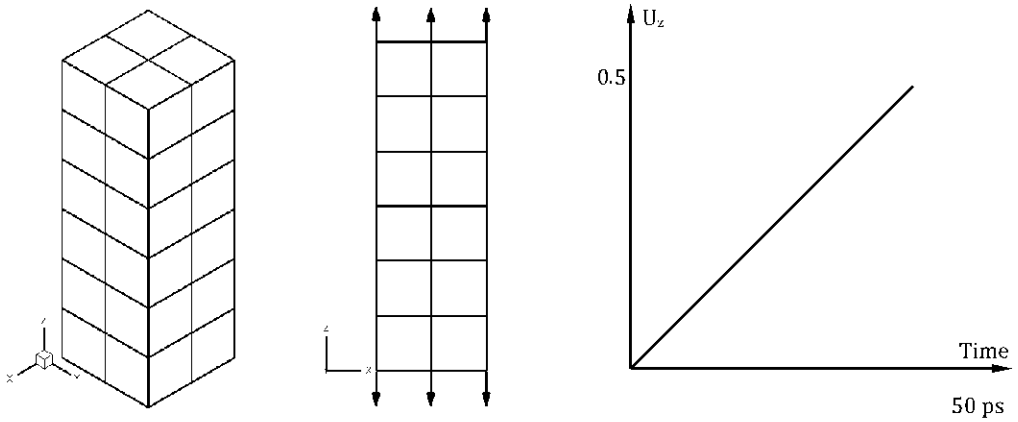

(a) Finte Element Mesh (b) Loading history and boundary

Figure 7: Computational model of MgO specimen under uniaxial tension

gate to the middle of specimen, and then they meet and separate. In this example, through the simulations of a complete circle of wave propagation (meeting, separation and reflection) the robustness and stability of the finite element implementation is demonstrated.

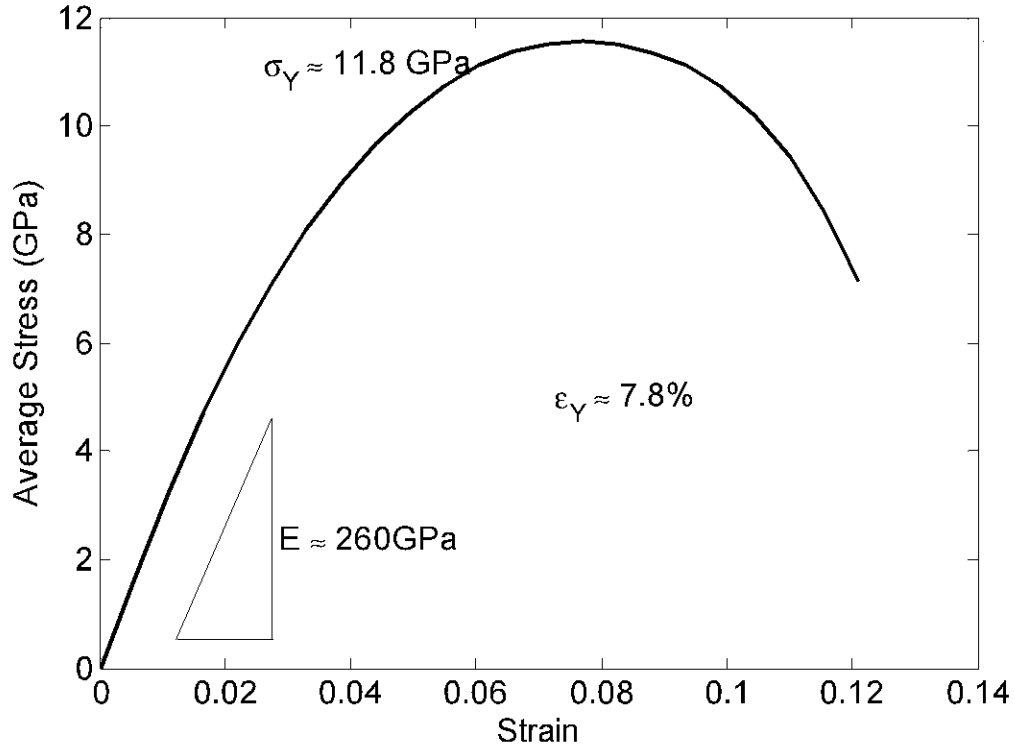

Figure 8: Stress-strain curve of MgO specimen under tension

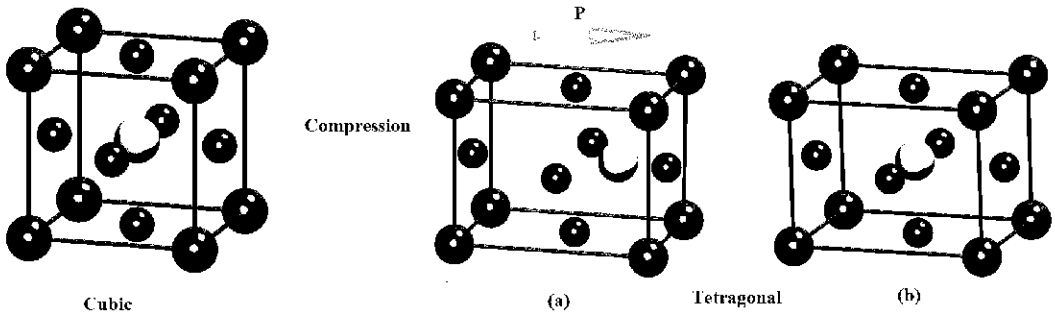

Figure 9: Polarization in $BaTiO_3$ under compressive strain

4.2 Uniaxial tension

Under uniaxial tension, a small MgO specimen (1.6 nm × 1.6 nm × 5 nm, 2600 atoms) is discretized into 24 elements. There are 63 FE nodes in the computational model. Thus the number of the degrees of freedom involved in ABC method is about 2.4% of that in MD. In the simulation of MgO under tension, displacement

controlled boundary conditions with a constant velocity 10m/s are applied on the two ends and the total loading time is 50 ps (Fig. 7 b). The stress-strain curve obtained is plotted in Fig. 8. Here, the stress is calculated as the average of all unit cells. Fig. 8 shows a rapid stress increase up to the maximum tensile strength followed by a drop when the specimen is going to fail; notice that the applied elongation is still increasing. This is similar to the conventional tensile testing: the stress-strain curve is essentially smooth with a linear slope within elastic range. Both the linear elastic range and the yield point are visible. Young's modulus can be estimated as 260 GPa, which is higher than the bulk experimental value or the first principle value of 250 GPa. Yield strength is about 11.8 GPa and the yield strain is about 0.08. Those values are close to what have been reported in previous MD simulation (Xiong et al., 2006).

4.3 Polarization

Piezoelectric materials at nanoscale have attracted increasing attention due to their promising applications in piezoelectric motors, nanoactuators, nanogenerators, etc. Nanogenerators (Wang and Song, 2006) offer the potential of harvesting energy from the environment for self-powered nanosystems based on the piezoelectric effect, i.e., a mechanical stress/strain can be converted into polarizations in the material, thereby inducing an electric voltage.

The piezoelectric material BaTiO3 has a centrosymmetric cubic crystal structure as a reference nonpolar state, and polarization is defined with respect to the nonpolar state (Fig. 9) and is a function of internal atomic displacements. It is noticed in Fig.9 that the unit cell becomes tetragonal structure under the compressive strain. When the interior atoms are allowed to move independently, one may encounter a non-centrosymmetric structure which gives a polarization (Fig. 9a). On the other hand, if we follow Cauchy-Born rule strictly, then the tetragonal structure is still centrosymmetric and hence it yields no polarization (Fig. 9b). From Eq. (25), which governs the motion of every atom in unit cells, it is seen that the internal atomic displacements have been naturally incorporated in our formulations. In our ABC method, it is straightforward to show the polarization density $\mathbf{P}^k(t)$ of a lattice point as

$$\mathbf{P}^k(t) = \frac{1}{\Delta V}\sum_{\alpha=1}^{N_a} q^{k\alpha}\mathbf{x}^{k\alpha}(t) = \frac{1}{\Delta V}\sum_{\alpha=1}^{N_a} q^{k\alpha}(\mathbf{X}^k+\mathbf{u}^{k\alpha}(t)) = \frac{1}{\Delta V}\sum_{\alpha=1}^{N_a} q^{k\alpha}\mathbf{u}^{k\alpha}(t) \qquad (32)$$

where ΔV is the volume of a unit cell, $q^{k\alpha}$ is the charge of atom $k\alpha$.

In this numerical simulation, a nanosize BaTiO3 specimen (1.6 nm $\times$ 1.6 nm $\times$ 3.2 nm) subject to a compressive loading is modeled with 128 finite elements and

225 nodes. The displacement controlled boundary conditions with a constant velocity 30m/s are applied on the top end and the total loading time is 10 ps (Fig. 10). As shown in Fig. 9, when the specimen is subject to a compressive loading in the z-direction, an expected polarization will appear in the x-y plane. Here we define $P_\perp = \sqrt{\mathbf{P}_x \cdot \mathbf{P}_x + \mathbf{P}_y \cdot \mathbf{P}_y}$to characterize the magnitude of the polarization on the x-y plane. Fig. 11 shows the contour plots of polarization $P_\perp$ with time evolution. It is seen that the polarization $P_\perp$ become more pronounced as time goes. It is observed that the polarizations $P_\perp$easily appear at the edges since the symmetry of unit cell is more vulnerable to break under the compression loading. Also, polarizations accompany the phenomenon of bulging.

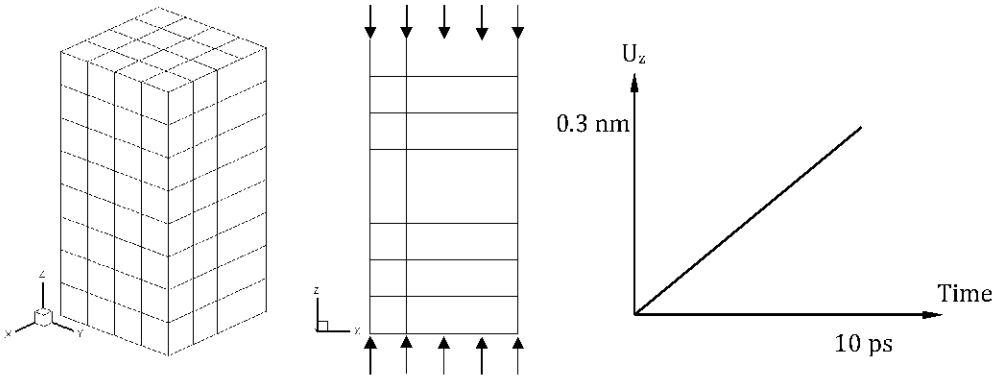

Figure 10: Computation model: (a) Finite element mesh; (b) Boundary conditions; (c) Loading history

5 Concurrent atomistic/continuum simulation

In this section, we simulate 3D dynamic fracture as a benchmark problem for concurrent atomistic/continuum modeling and simulation in order to show the advantage of our method. Dynamic crack propagation is a paradigm for concurrent multiscale methods, since it contains a critical region of confined size, that requires fully atomistic resolution enabling crack initiation and, on the other hand, a coarse-graining for an efficient representation of continuum region in the crystal. A specimen (cf. Fig. 12) made of MgO (25.2 nm $\times$ 0.9 nm $\times$ 15.1 nm, 54,048atoms) consists of two parts: continue region (234 FE elements and 444 FE nodes) and atomic region (6216 atoms). Thus the number of the degrees of freedom involved in continuum region is about 1% of that in MD. The line crack extends from $x = 0$ to $x = 2.3$ nm at $z = 0$ through $y \in (0,\ 0.9\text{ nm})$; and the separation of crack surfaces is 0.9 nm. This means, in order to simulate the crack, two planes of atoms parallel to the crack surfaces are eliminated from the compact tension specimen. In the

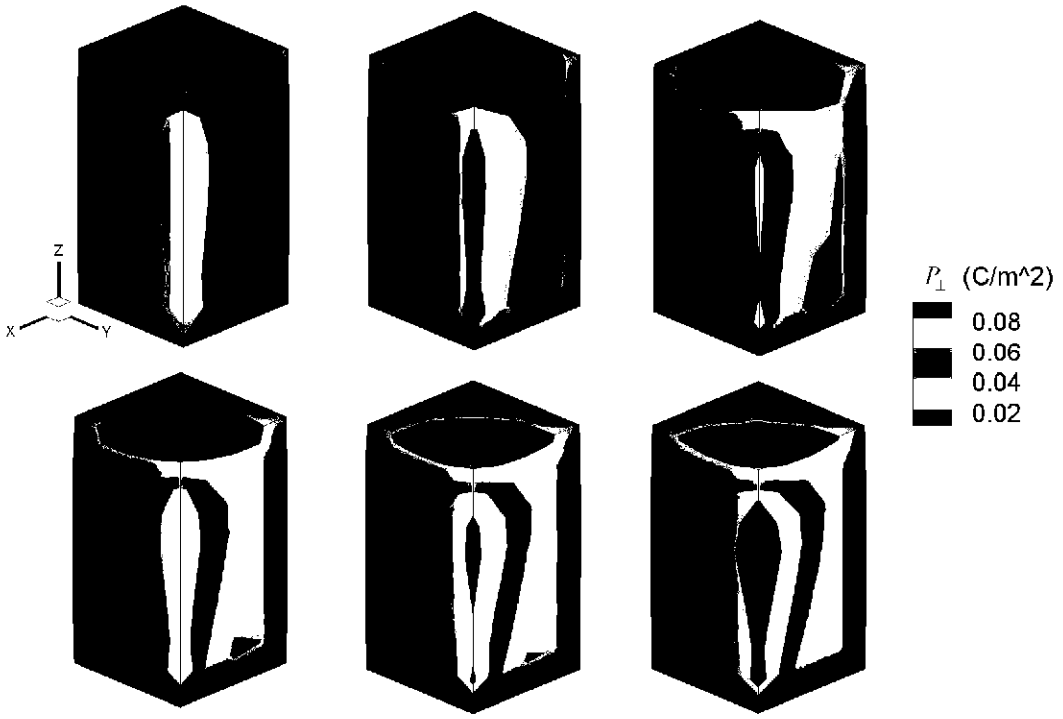

Figure 11: Polarization $P_\perp$ evolution with time

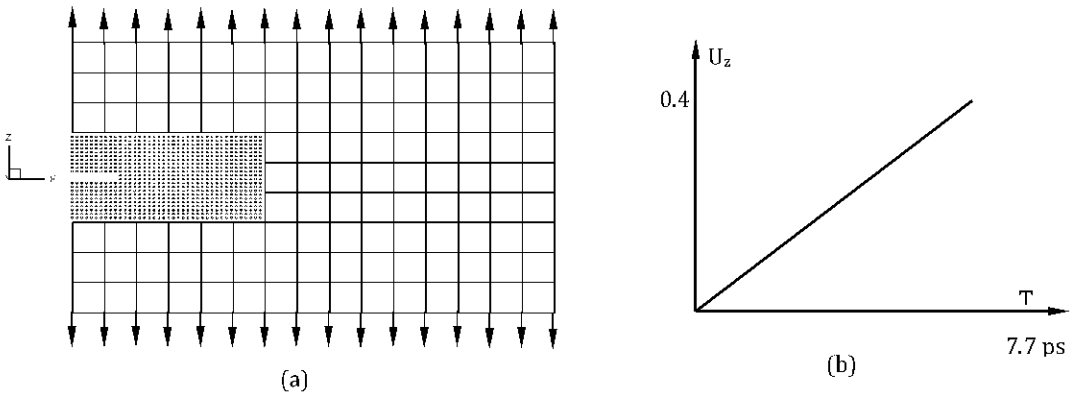

Figure 12: Computational model of MgO specimen for dynamic crack: (a) FE and Atom arrangement model; (b) loading history

simulation, displacement controlled boundary conditions with a constant loading rate 50m/s are applied on the two surfaces $z = -7.55$ nm and $z = 7.55$ nm and the total loading time is 7.7 ps (Fig.12).

Fig. 13 shows the process of dynamic crack propagation in the neighborhood of

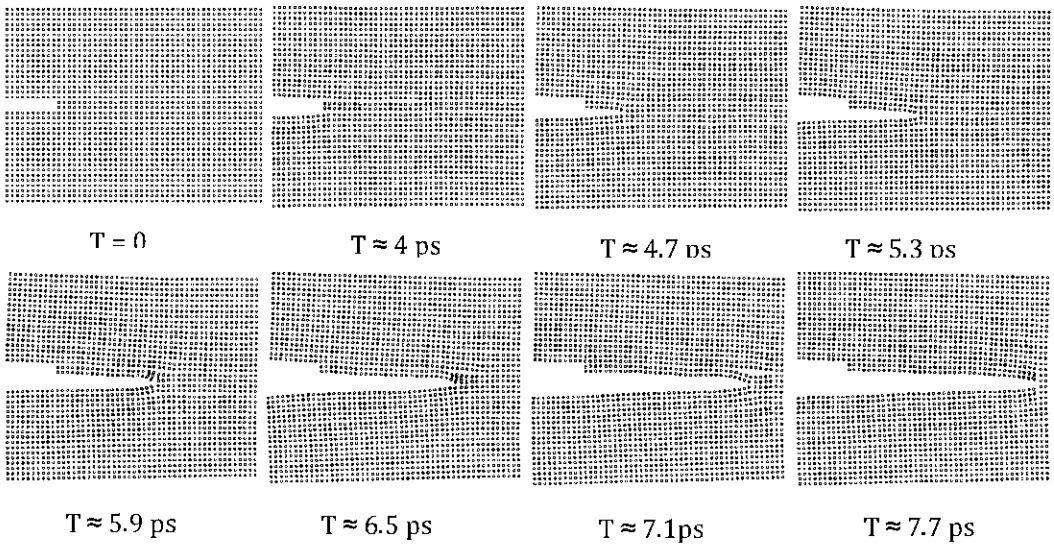

Figure 13: Crack initiation and propagation in MgO specimen

crack-tip. It is noticed that the crack propagates along the direction of the original line crack self-similarly, in other words, it propagates along the same crystallographic planes. This observation agrees with experimental studies by Cramer (2000). This is mainly because MgO is in the cubic phase and this specimen and the loading condition have a nearly perfect mirror symmetry with respect to the x-y plane. We also observe that the formation of secondary cracks in front of the primary crack. Similar phenomena in silicon have been reported by Buehler et al. (2006).

6 Summary

We have presented an atom-based continuum (ABC) method aiming at a seamless transition from atomistic to the continuum description of multi-element crystalline solids. The finite element implementation and numerical procedure have been developed with a cluster-based summation rule in interatomic force calculation.

Compared with many other concurrent multiscale approaches, ABC method is naturally suitable for the analysis of multi-element crystals. The fundamental independent unknown variables are the displacements of all atoms within the FE nodes. Notice that there is a superscript α in the governing equation, Eq. (25). It is the very superscript that makes our ABC method quite different from the classical continuum field theories.

To consolidate the competition between efficiency and accuracy just like many other multiscale approaches, we adopt a cluster-based summation rule for force calculation in the FE formulation. Notice that our summation rule is a general one, which enables one to choose the weighting factor from one extreme to the other.

The robustness and stability of the coarse-graining method by employing a nodal integration scheme have been demonstrated through the simulation of dynamic wave propagation.

In the coarse-scale simulations, the majority of degrees of freedom are eliminated and the computation cost is largely reduced. Nevertheless, the essential dynamic, nonlinear, nonlocal, and large-deformation material behaviors have been successfully presented.

Polarization has been reported in the coarse-scale simulations of $BaTiO_3$ under compressive loading. This shows an advantage of ABC over classical continuum mechanics and other multiscale approaches in capturing the critical material behaviors such as polarization.

In a dynamic crack simulation, we have demonstrated that the ABC method can be extended to the level of concurrent atomistic/continuum modeling. Crack initiation and propagation have been captured in the atomic region. This indicates that our approach can be utilized to investigate critical phenomena in material bodies with finite sizes.

References

Abraham, F.F., Broughton, J.Q., Bernstein, N., Kaxiras, E. (1998): Spanning the continuum to quantum length scales in a dynamic simulation of brittle fracture. *Europhys. Lett.* 44, 783-787.

Belytschko, T., Xiao, S. P. (2003): Coupling methods for continuum model with molecular model. *J. Mult. Comput. Engrg.* 1, 115-126.

Buehler, M.J., van Duin, A.C.T., Goddard III, W.A. (2006): Multiparadigm modeling of dynamical crack propagation in silicon using a reactive force field. *Physical Review Letters*, 96(9), 095505.

Crammer, T., Wanner, A., Gumbsch, P. (2000): Energy Dissipation and Path Instabilities in Dynamic Fracture of Silicon Single Crystals, *Phys. Rev. Lett.*, 85, 788.

Eidel, B., Stukowski, A. (2009): A variational formulation of the quasicontinuum method based on energy sampling in clusters. *J. Mech. Phys. Solids*, 57, 87-108.

Fish, J., Nuggehally, M.A., Shephard, M.S., Picu, C.R., Badia, S., Parks, M.L., Gunzburger, M. (2007): Concurrent AtC coupling based on a blend of the contin-

uum stress and the atomistic force. *Computer Methods in Applied Mechanics and Engineering*, 196(45-48), 4548–4560.

Goldstein, H. (1950): *Classical Mechanics*, Addison-Wesley, Reading, Mass.

Grimes, R.W. (1994): Solution of MgO, CaO and TiO_2 in α-Al_2O_3. *J. Am. Ceram. Soc.* 77, 378.

Knap, J., Ortiz, M. (2001): An analysis of the quasicontinuum method. *J. Mech. Phys. Sol.*, 49, 1899–1923.

Ma, J.; Lu, H.; Wang, B.; Hornung, R.; Wissink, A.; Komanduri, R. (2006): Multiscale Simulation Using Generalized Interpolation Material Point (GIMP) Method and Molecular Dynamics (MD), *CMES: Computer Modeling in Engineering & Sciences*, vol. 14 (2), 101-118.

Parks, M.L., Bochev, P.B., Lehoucq, R.B. (2008): Connecting atomistic-to-continuum coupling and domain decomposition. *Multiscale Modeling & Simulation*, 7(1), 362–380.

Raghavan, P.; Ghosh, S. (2004): Adaptive multiscale computational modeling of composite materials, *CMES: Computer Modeling in Engineering and Science* vol.5, 151-170.

Rudd, R.E., Broughton, J.Q. (2001): Concurrent coupling of length scales in solid state systems. *Phys. Status Solidi B*, 217, 251-291.

Shen, S.; Atluri, S.N. (2004a): Multiscale simulation based on the meshless local Petrov-Galerkin (MLPG) method, *CMES: Computer Modeling in Engineering & Sciences* , vol. (3), 235-255.

Shen, S.; Atluri, S.N. (2004b): Computational nano-mechanics and multi-scale simulation, *CMC: Computers, Materials & Continua* 1vol. (1), 59-90.

Shen, S.; Atluri, S.N. (2004c): Atomic-level stress calculation and continuum-molecular system equivalence, *CMES: Computer Modeling in Engineering & Sciences* vol. 6 (1), 91-104.

Steinmann, P., Elizondo, A., Sunyk, R. (2006): Studies of validity of the Cauchy-Born rule by direct comparison of continuum and atomistic modeling. *Modelling Simul. Mater. Sci. Eng.*, 15, 271-281.

Tadmor, E. B., Ortiz, M., Phillips, R. (1996): Quasicontinuum analysis of defects in solids. *Philo. Mag.*, 73, 1529-1563.

Tadmor, E. B., Smith, G.S., Bernstein, N., Kaxiras, E. (1999): Mixed finite element and atomistic formulation for complex crystals. *Physical Review B*, 59, 235-245.

Wagner, G.J., Liu, W.K. (2003): Coupling of atomistic and continuum simula-

tions using a bridging scale decomposition. *J. Comput. Phys.*, 190, 249–274.

Wang, Z.L., Song, J. H. (2006): Piezoelectric nanogenerator based on zinc oxide nanowire arrays. *Science*, 14, 242-246.

Woodley, S.W., Battle, P. D., Gale, J. D., Catlow, C.R.A. (1999): *Phys. Chem.*, 1, 2535-2542.

Xiao, S. P., Belytschko, T. (2004): A bridging domain method for coupling continua with molecular dynamics. *Comput. Methods Appl. Mech. Engrg.*, 193, 1645-1669.

Xiong, L., Chen, Y., Lee, J.D. (2006): Atomistic measure of the strength of MgO nanorods. *Theoretical and Applied Fracture Mechanics*, 46, 202–208.

Appendix A

The Lagrange equation of the atomic systems is written as

$$\frac{d}{dt}\left(\frac{\partial L}{\partial \dot{\mathbf{x}}^{m\gamma}}\right)-\frac{\partial L}{\partial \mathbf{x}^{m\gamma}}+\frac{\partial D}{\partial \dot{\mathbf{x}}^{m\gamma}}=\varphi^{m\gamma} \tag{A1}$$

It is straightforward to obtain

$$\begin{aligned}\frac{\partial L}{\partial \dot{\mathbf{x}}^{m\gamma}}&=\frac{\partial K}{\partial \dot{\mathbf{x}}^{m\gamma}}=\frac{1}{2}\frac{\partial}{\partial \dot{\mathbf{x}}^{m\gamma}}\{\sum_k\sum_\alpha m^\alpha(\dot{\mathbf{x}}^{k\alpha})^2\}\\&=\sum_k\sum_\alpha m^\alpha\dot{\mathbf{x}}^{k\alpha}\delta_{km}\delta_{\alpha\gamma}\\&=m^\gamma\dot{\mathbf{x}}^{m\gamma}\end{aligned} \tag{A2}$$

$$\frac{d}{dt}\left(\frac{\partial L}{\partial \dot{\mathbf{x}}^{m\gamma}}\right)=m^\gamma\ddot{\mathbf{x}}^{m\gamma} \tag{A3}$$

$$\begin{aligned}-\frac{\partial L}{\partial \mathbf{x}^{m\gamma}}&=\frac{\partial V}{\partial \mathbf{x}^{m\gamma}}=\frac{\partial}{\partial \mathbf{x}^{m\gamma}}\{\frac{1}{2}\sum_k\sum_\alpha\sum_l\sum_\beta V^{k\alpha-l\beta}(\mathbf{x}^{k\alpha},\mathbf{x}^{l\beta})\}\\&=\frac{1}{2}\sum_k\sum_\alpha\sum_l\sum_\beta\{\frac{\partial V^{k\alpha-l\beta}}{\partial \mathbf{x}^{k\alpha}}\delta_{mk}\delta_{\gamma\alpha}+\frac{\partial V^{k\alpha-l\beta}}{\partial \mathbf{x}^{l\beta}}\delta_{ml}\delta_{\gamma\beta}\}\\&=\frac{1}{2}\sum_l\sum_\beta\frac{\partial V^{m\gamma-l\beta}}{\partial \mathbf{x}^{m\gamma}}+\frac{1}{2}\sum_k\sum_\alpha\frac{\partial V^{k\alpha-m\gamma}}{\partial \mathbf{x}^{m\gamma}}\\&=-\frac{1}{2}\sum_l\sum_\beta\{\mathbf{f}^{m\gamma-l\beta}-\mathbf{f}^{l\beta-m\gamma}\}\end{aligned} \tag{A4}$$

$$\begin{aligned}\frac{\partial D}{\partial \dot{\mathbf{x}}^{m\gamma}} &= \frac{1}{2}\frac{\partial}{\partial \dot{\mathbf{x}}^{m\gamma}}\{\sum_k\sum_\alpha m^\alpha(\dot{\mathbf{x}}^{k\alpha})^2\}/\tau \\ &= m^\gamma \dot{\mathbf{x}}^{m\gamma}/\tau\end{aligned} \tag{A5}$$

Finally one has

$$m^\gamma \ddot{\mathbf{x}}^{m\gamma} + \frac{m^\gamma}{\tau}\dot{\mathbf{x}}^{m\gamma} = \frac{1}{2}\sum_l\sum_\beta\{\mathbf{f}^{m\gamma-l\beta} - \mathbf{f}^{l\beta-m\gamma}\} + \varphi^{m\gamma} \tag{A6}$$

Appendix B

The weak form of the atomic system is given as

$$\begin{aligned}&\sum_k\sum_\alpha m^\alpha \ddot{\mathbf{u}}^{k\alpha}\delta\mathbf{u}^{k\alpha} + \sum_k\sum_\alpha c^\alpha \dot{\mathbf{u}}^{k\alpha}\delta\mathbf{u}^{k\alpha} \\ &= \frac{1}{2}\sum_k\sum_\alpha\sum_l\sum_\beta \mathbf{f}^{k\alpha-l\beta}\{\delta\mathbf{u}^{k\alpha} - \delta\mathbf{u}^{l\beta}\} + \sum_k\sum_\alpha \varphi^{k\alpha}\delta\mathbf{u}^{k\alpha} \\ &A + B = C + D\end{aligned} \tag{B1}$$

$$\begin{aligned}A &= \sum_I\sum_J\sum_k\sum_\alpha m^\alpha \mathbf{\Phi}_J(k)\ddot{\mathbf{U}}_J^\alpha \mathbf{\Phi}_I(k)\delta\mathbf{U}_I^\alpha \\ &= \sum_I\sum_\alpha \delta\mathbf{U}_I^\alpha\{\sum_J\sum_k m^\alpha \mathbf{\Phi}_J(k)\mathbf{\Phi}_I(k)\ddot{\mathbf{U}}_J^\alpha\} \\ &= \sum_I\sum_\alpha \delta\mathbf{U}_I^\alpha\{\sum_J\sum_k m^\alpha \mathbf{\Phi}_J(k)\mathbf{\Phi}_I(k)\}\ddot{\mathbf{U}}_J^\alpha \\ &\equiv \sum_I\sum_\alpha \delta\mathbf{U}_I^\alpha\{\sum_J M_{IJ}^\alpha\}\ddot{\mathbf{U}}_J^\alpha\end{aligned} \tag{B2}$$

$$\begin{aligned}B &= \sum_I\sum_J\sum_k\sum_\alpha c^\alpha \mathbf{\Phi}_J(k)\dot{\mathbf{U}}_J^\alpha \mathbf{\Phi}_I(k)\delta\mathbf{U}_I^\alpha \\ &= \sum_I\sum_\alpha \delta\mathbf{U}_I^\alpha\{\sum_J\sum_k c^\alpha \mathbf{\Phi}_J(k)\mathbf{\Phi}_I(k)\dot{\mathbf{U}}_J^\alpha\} \\ &= \sum_I\sum_\alpha \delta\mathbf{U}_I^\alpha\{\sum_J\sum_k c^\alpha \mathbf{\Phi}_J(k)\mathbf{\Phi}_I(k)\}\dot{\mathbf{U}}_J^\alpha \\ &\equiv \sum_I\sum_\alpha \delta\mathbf{U}_I^\alpha\{\sum_J C_{IJ}^\alpha\}\dot{\mathbf{U}}_J^\alpha\end{aligned} \tag{B3}$$

$$
\begin{aligned}
C &= \frac{1}{2}\sum_k\sum_\alpha\sum_l\sum_\beta \mathbf{f}^{k\alpha-l\beta}\{\sum_I \mathbf{\Phi}_I(k)\delta\mathbf{U}_I^\alpha - \sum_K \mathbf{\Phi}_K(l)\delta\mathbf{U}_K^\beta\} \\
&= \sum_I\sum_\alpha \delta\mathbf{U}_I^\alpha\{\frac{1}{2}\sum_k\sum_l\sum_\beta \mathbf{f}^{k\alpha-l\beta}\mathbf{\Phi}_I(k)\} \\
&+ \sum_K\sum_\beta \delta\mathbf{U}_K^\beta\{-\frac{1}{2}\sum_k\sum_l\sum_\alpha \mathbf{f}^{k\alpha-l\beta}\mathbf{\Phi}_K(l)\} \\
&= \sum_I\sum_\alpha \delta\mathbf{U}_I^\alpha\{\frac{1}{2}\sum_k\sum_l\sum_\beta \mathbf{f}^{k\alpha-l\beta}\mathbf{\Phi}_I(k)\} \\
&+ \sum_I\sum_\alpha \delta\mathbf{U}_I^\alpha\{-\frac{1}{2}\sum_k\sum_l\sum_\gamma \mathbf{f}^{k\gamma-l\alpha}\mathbf{\Phi}_I(l)\} \\
&\equiv \sum_I\sum_\alpha \delta\mathbf{U}_I^\alpha\mathbf{F}_I^\alpha
\end{aligned}
\tag{B4}
$$

$$
\begin{aligned}
D &= \sum_k\sum_\alpha\sum_I \varphi^{k\alpha}\mathbf{\Phi}_I(k)\delta\mathbf{U}_I^\alpha \\
&= \sum_I\sum_\alpha \delta\mathbf{U}_I^\alpha\sum_k \varphi^{k\alpha}\mathbf{\Phi}_I(k) \\
&\equiv \sum_I\sum_\alpha \delta\mathbf{U}_I^\alpha\varphi_I^\alpha
\end{aligned}
\tag{B5}
$$

Then the governing equations for nodal displacements $\mathbf{U}_I^\alpha$ can be expressed

$$
\left(\sum_J M_{IJ}^\alpha\right)\ddot{\mathbf{U}}_J^\alpha + \left(\sum_J C_{IJ}^\alpha\right)\dot{\mathbf{U}}_J^\alpha = \mathbf{F}_I^\alpha + \varphi_I^\alpha \tag{B6}
$$